Anomalous sharp peak in the London penetration depth induced by the nodeless-to-nodal superconducting transition in $BaFe_2(As_{1-x}P_x)_2$

Huai-Xiang Huang,[1,*] Wei Li,[2,3,†] Yi Gao,[4] Yan Chen,[2,3] and Fu-Chun Zhang[5,3]

[1]*Department of Physics, Shanghai University, Shanghai 200444, China*

[2]*State Key Laboratory of Surface Physics and Department of Physics, Fudan University, Shanghai 200433, China*

[3]*Collaborative Innovation Center of Advanced Microstructures, Nanjing University, Jiangsu 210093, China*

[4]*Department of Physics and Institute of Theoretical Physics, Nanjing Normal University, Nanjing, Jiangsu 210023, China*

[5]*Kavli Institute for Theoretical Sciences and CAS Center for Excellence in Topological Quantum Computation, University of Chinese Academy of Sciences, Beijing 100190, China*

(Received 30 November 2018; revised manuscript received 26 August 2019; published 1 October 2019)

The issue of whether the quantum critical point (QCP) is hidden inside unconventional superconductors is a matter of hot debate. Although a prominent experiment on London penetration depth has demonstrated the existence of the QCP in the isovalent-doped iron-based superconductor $BaFe_2(As_{1-x}P_x)_2$, with the observation of a sharp peak in the penetration depth in the vicinity of the disappearance of magnetic order at zero temperature, the nature of such an emerging QCP remains unclear. Here, we provide a unique picture to understand well the phenomena of the QCP based on the framework of linear response theory. Evidence from the density of states and superfluid density calculations suggests the nodeless-to-nodal pairing transition accompanied the appearance of a sharp peak in the penetration depth in $BaFe_2(As_{1-x}P_x)_2$. Such a pairing transition originates from the three-dimensional electronic properties with a strong interlayer superconducting pairing. This finding provides a significant insight into the understanding of the QCP observed in experiment in $BaFe_2(As_{1-x}P_x)_2$.

DOI: 10.1103/PhysRevB.100.144501

I. INTRODUCTION

Studies of unconventional iron-based superconductivity have triggered intensive research interest during the past decade since the discovery of $LaO_{1-x}F_xFeAs$ in 2008 [1]. For low-energy electronic properties, iron-based materials are a multiband system with nodeless $s_{\pm}$-wave superconducting pairing symmetry [2,3] in contrast to that of cuprates, which are a single-band system with nodal d-wave superconducting pairing symmetry [4,5]. Despite such differences at the microscopic level, the layered crystal structure and phase diagram of both iron-based and copper oxide superconductors share a common feature. From the viewpoint of the superconducting phase diagram, those compounds exhibit similar dome-shaped superconductivity after introducing the extra electron or hole-like charge carriers into the parent compound or applying high external pressure or chemical pressure. An isovalent phosphorus substitution of arsenic in the $BaFe_2(As_{1-x}P_x)_2$ compound accompanied by the appearance of superconductivity [6–11] can be regarded as a kind of chemical pressure. Importantly, a prominent experiment on London penetration depth in this compound observed a sharp peak in the vicinity of the disappearance of magnetic order at zero temperature, suggesting the presence of a quantum critical point (QCP) [12] and attracting widespread research attention [13–17].

Elucidating the origin of such a QCP inside the superconducting dome could be the key to understanding high-temperature superconductivity [17–23]. Since the parent compound of $BaFe_2As_2$ has a collinear antiferromagnetic order, tuning the electronic band structure by introducing isovalent phosphorus dopants without introducing charge carriers will suppress the magnetic order, and superconductivity will emerge. This leads to conjecture regarding whether the disappearance of magnetic order will be associated with a sharp peak in the superfluid density in the London penetration depth experiment [12,13]. A previous theoretical study demonstrated that in two-dimensional systems the concentration of superfluid density, which is proportional to the London penetration depth, $\rho_s \propto 1/\lambda_L^2$, monotonically increases with the suppression of the magnetic order in the region where magnetism and superconductivity coexist, until the superfluid density saturates to a maximal value in a pure superconducting region in Fe-based superconductors [24]. Therefore, such conjecture seems to be insufficient to explain the nature of the London penetration depth experiment, and various theoretical scenarios are proposed to explain the possible nature of such an anomalous enhancement of λ_L [17,25–27].

Fortunately, angle-resolved photoemission spectroscopy (ARPES) measurements of the superconducting gap structure of $BaFe_2(As_{0.7}P_{0.3})_2$ demonstrated the direct observation of a circular line node on the most significant hole Fermi surface around the Z point at the Brillouin zone boundary [28]. This finding opens an avenue for conjecturing whether the QCP observed in the penetration depth experiment is closely related to such nodal pairing structure. In addition, the ARPES experiment and the first-principles calculations also suggested that the Fermi surface topology becomes much more three-dimensional with increasing the phosphorus

*hxhuang@shu.edu.cn

†w_li@fudan.edu.cn

dopants [7,12,28–30], leading us to establish a perspective of the nodeless-to-nodal pairing transition accompanied by the appearance of a QCP in $BaFe_2(As_{1-x}P_x)_2$, which is the primary motivation of the present paper.

In this paper, a doping-dependent three-dimensional tight-binding model is constructed to reproduce well the correct low-energy electronic band structure and the Fermi surface topologies from ARPES measurements [7]. By taking the Coulomb interactions between itinerant electrons into account, we perform self-consistent mean-field calculations and obtain a phase diagram of pairing order parameters versus doping concentrations, which is in agreement with experiments [12]. Further calculations of superfluid density and the density of states (DOS) as a function of doping demonstrate that the appearance of a sharp peak in the penetration depth is accompanied by a nodeless-to-nodal pairing transition. Such a superconducting pairing transition mainly comes from the nature of the three-dimensional electronic band structure with strong interlayer superconducting pairing order. Additionally, it is worth pointing out that the calculated maximum λ_L does not appear at the transit point of the magnetic order observed by experiment [12]; instead, it is within the overlapping range of spin-density wave and superconducting phases. The same feature was reported in a previous work by using the universal critical phenomena theory, which indicated that the possible explanation of the discrepancy between experiment observation and theoretical calculation requires the consideration of the physical properties at the scale of the correlation length or an even smaller length scale.

The rest of this paper is organized as follows. In Sec. II, we first introduce the theoretical model Hamiltonian and the methods of the detailed calculations. The calculated phase diagram, superfluid density, and London penetration depth at zero temperature are given in Sec. III. In Sec. IV, the DOS and Fermi surface of the superconducting state are addressed. A summary is finally given in Sec. V.

II. MODEL HAMILTONIAN

According to the fact of experimental measurements [7,12], we extend the two-dimensional phenomenological model with two orbitals [31] to a three-dimensional model with three orbitals to study the superconducting electronic properties in isovalent-doped $BaFe_2(As_{1-x}P_x)_2$. The previous two-dimensional model considered the effect of the asymmetric arsenic atoms and is appropriate to describe the experimental observations in ARPES and scanning tunnel microscope for the 122 family [32–35]. The calculated superfluid density is in qualitative agreement with the direct experimental measurement in films of Fe pnictide superconductors at low temperatures [36]. In the extended model, a unit cell contains two Fe atoms, and each Fe involves three orbitals, d_{xz}, d_{yz}, and d_{z^2}. As arsenic is gradually substituted by phosphorus, the d_{z^2} orbital of Fe will be driven close to the Fermi level [29,37], resulting in an enhancement of interlayer hybridization between two interlayer Fe orbitals.

In Fig. 1(a), we show a schematic illustration of the tight-binding model Hamiltonian in real space, where t'_{1-4} are hopping energies within each Fe layer between d_{xz} and d_{yz} orbitals. Here, it should be noted that t'_2 is different from t'_3 since asymmetric arsenic ions is above and below the Fe layer alternatively [31]. $t'_{z,s,u}$ are the interlayer hopping energies between two adjacent Fe layers. t'_z denotes the nearest-neighbor hopping energy along the z axis between d_{z^2} and d_{xz} (d_{yz}) orbitals, which can be regarded as two-step hopping processes $c^\dagger_{i+z}A_{i+z/2}A^\dagger_{i+z/2}c_i$ + H.c. mediated by arsenic (denoted by A) in the crystal structure environment of $BaFe_2(As_{1-x}P_x)_2$.

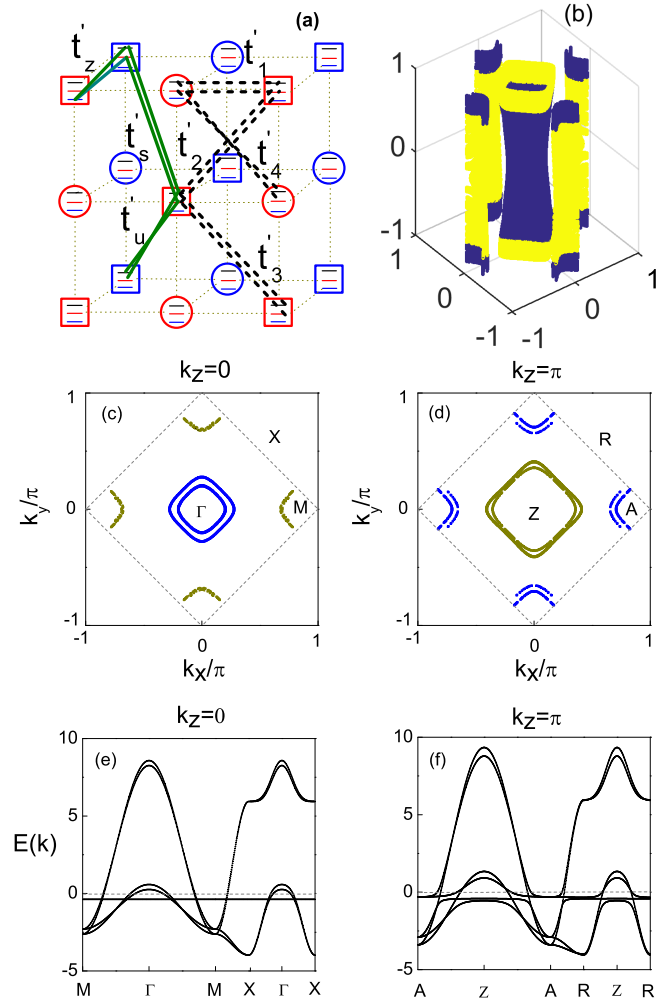

FIG. 1. (a) Schematic illustration of hopping energy parameters of the three-dimensional tight-binding model $-t_{ij}c^\dagger_i c_j$ [i denotes all the indexes of site i] with three Fe orbitals, d_{xz}, d_{yz}, and d_{z^2}, in real space. The red symbols denote the sites in one Fe layer, and the blue symbols denote those in the adjacent Fe layer. The two inequivalent Fe atoms are denoted by circles and squares. Hopping in the same layer is linked by black dashed lines, while hopping between adjacent layers is linked by solid olive lines. (b) The three-dimensional Fermi surface topologies of $BaFe_2(As_{1-x}P_x)_2$ for $x = 0.18$. The label of the space axes is $k_{i=x,y,z}/\pi$. For the three-dimensional Fermi surface topologies, blue (yellow) points represent plus (minus) signs of superconducting order in the band space, which appears after introducing the interactions. The contour plot of the three-dimensional Fermi surface structure (c) for $k_z = 0$ and (d) for $k_z = \pi$. The dashed lines denote the first Brillouin zone with two Fe atoms per unit cell. The band structure is plotted along the high-symmetry **k** points for (e) $k_z = 0$ and (f) $k_z = \pi$. The gray dashed line denotes the Fermi level.

Under the C_2 rotation at site i, $c^\dagger_{i+z,\beta\sigma}A_{i+z/2} \longrightarrow -c^\dagger_{i-z,\beta}A_{i-z/2\sigma}$, the combination of $c^\dagger_{i+z,\beta\sigma}A_{i+z/2} - c^\dagger_{i-z,\beta\sigma}A_{i-z/2}$ will replace the hopping term $c^\dagger_{i+z}A_{i+z/2}$ [37,38], and thus, the two-step hopping processes become $-4t_z \sin^2 k_z$ after omitting the creation and annihilation operators of arsenic. t_s' (t_u') is the hopping energy along $\hat{x} \pm \hat{y} \pm \hat{z}$ between the same (different) d_{xz}, d_{yz} orbitals in two adjacent Fe layers. Using the Fourier transformation, the tight-binding model Hamiltonian in momentum space can be rewritten as

$$H_{t,k} = \sum_{k\nu\sigma R} a_1 c^\dagger_{A\nu\sigma k} c_{A\nu\sigma k} + a_2 c^\dagger_{B\nu\sigma k} c_{B\nu\sigma k} + a_3 c^\dagger_{R\nu\sigma k} c_{R\bar{\nu}\sigma k} + a_4 c^\dagger_{A\nu\sigma k} c_{B\nu\sigma k} + a_5 c^\dagger_{R\nu\sigma k} c_{R\beta\sigma k} + \text{H.c.}, \quad (1)$$

where $R = A, B$ denotes two inequivalent sites of Fe atoms, ν denotes the d_{xz}, d_{yz} orbitals, β is the d_{z^2} orbital, and σ is the spin. Comparing hopping terms in k space with the hopping parameters in real space, we obtain the coefficients in model Hamiltonian as follows:

$$\begin{aligned}
a_1 &= -2t_2 \cos(k_x + k_y) - 2t_3 \cos(k_x - k_y) \\
&\quad - 2t_s(1 - \cos k_z)[\cos(k_x + k_y) + \cos(k_x - k_y)], \\
a_2 &= -2t_3 \cos(k_x - k_y) - 2t_2 \cos(k_x + k_y) \\
&\quad - 2t_s(1 - \cos k_z)[\cos(k_x + k_y) + \cos(k_x - k_y)], \\
a_3 &= -2t_4[\cos(k_x + k_y) + \cos(k_x - k_y)] \\
&\quad - 2t_u(1 - \cos k_z)[\cos(k_x + k_y) + \cos(k_x - k_y)], \\
a_4 &= -2t_1(\cos k_x + \cos k_y), \\
a_5 &= -2t_z(1 - \cos k_z),
\end{aligned}$$

with $t_{2,3} = t'_{2,3} - t_s, t_4 = t'_4 - t_u, t_{z,s,u} = -2t'_{z,s,u}, t_1 = t'_1$, as shown in Fig. 1(a).

Diagonalizing the model Hamiltonian (1), we plot the three-dimensional Fermi surface topology, as shown in Fig. 1(b). There are two quasicylindrical shells around the Γ point and two quasicylindrical shells around the M point. Figure 1(b) also shows the variation of the three-dimensional Fermi surface along the z direction, which is quite different from that in LaOFeAs superconductors [39]. For more detail, we depict the contour plots of the three-dimensional Fermi surface for $k_z = 0$ and $k_z = \pi$ in Figs. 1(c) and 1(d), respectively. The two Fermi surface circles around the Γ point are enlarged; in particular, the inner circle grows significantly with increasing k_z along the z direction, while the variation of cylindrical shells around the M points is insignificant. Those low-energy electronic behaviors are in good agreement with previous ARPES measurements [7,12]. In addition, the corresponding electronic band structures $E(k_x, k_y, k_z)$ are plotted for $k_z = 0$ and $k_z = \pi$, respectively, in Figs. 1(e) and 1(f) along the high-symmetry $\mathbf{k}$ points. For the tight-binding model, there are six bands, where the two bands of the d_{z^2} orbital are degenerate and dispersive below the Fermi level for $k_z = 0$, as shown in Fig. 1(e). However, for a finite k_z, the two degenerate flat bands will be split and become much more dispersive, which can be seen clearly in Fig. 1(f).

Taking the strong Coulomb interactions between itinerant electrons in Fe three-dimensional (3D) orbitals into account, we write the interaction Hamiltonian on a mean-field level as $H_{\text{int}} = H^{xy}_{\text{int}} + H^{z}_{\text{int}}$, which is expressed as [40–42]

$$\begin{aligned}
H^{xy}_{\text{int}} &= U\sum_{i\sigma\nu}\langle n_{i\nu\bar{\sigma}}\rangle n_{i\nu\sigma} + (U - 3J_H)\sum_{i\nu\sigma}\langle n_{i\nu\sigma}\rangle n_{i\nu\sigma} \\
&\quad + (U - 2J_H)\sum_{i\nu\sigma}\langle n_{i\nu\bar{\sigma}}\rangle n_{i\nu\sigma} - \sum_{i\nu\sigma}\mu n_{i\nu\sigma}, \quad (2)
\end{aligned}$$

$$\hat{H}^{z}_{\text{int}} = \sum_{i\sigma} U_z\langle n_{i\beta\sigma}\rangle n_{i\beta\bar{\sigma}} - \mu_1 n_{i\beta\sigma}, \quad (3)$$

where the parameter J_H denotes the Hund's coupling and U and U_z describe on-site Coulomb interaction on the d_{xz} (d_{yz}) and d_{z^2} orbitals, respectively. Since the d_{z^2} orbital is far below the Fermi level [29] in the parent compound $BaFe_2As_2$, without loss of generality, we set $\mu_1 = \mu + 1.36$ and search μ self-consistently to fix the total electron number as a constant (4 electrons/per Fe atom) throughout all calculations. All interactions and hopping parameters, such as t_2, t_3, and t_z, are doping dependent with fixed relations of $t_s = -t_z$, $t_u = 0.2t_z$, and $t_4 = 0.04$. The wave vector $\mathbf{k}$ is restricted in the magnetic Brillouin zone, ascribed to the system displaying a spin-density wave order. In addition, the local electron density is expressed as $n_{i\nu\sigma} = \frac{1}{4}\langle n_i\rangle + \sigma M_i$, and the magnetic order is described as $M = \frac{1}{2}\sum_\nu(n_{A\nu\uparrow} - n_{A\nu\downarrow}) = \frac{1}{2N_s}\sum_{\nu,\mathbf{k}}\sigma c^\dagger_{A\nu\sigma\mathbf{k}}c_{A\nu\sigma\mathbf{k}+\mathbf{Q}}$. Here N_s is the number of unit cells, and $Q = (0, \pm\pi)$ or $(\pm\pi, 0)$ is the wave vector of spin-density wave order [6].

Furthermore, we consider the intralayer and interlayer superconducting pairings between the same d_{xz} and d_{yz} orbitals as $H_\Delta = \sum_{R\nu\tau\tau'}\Delta^{R\nu}_{i,i+\tau}c^\dagger_{i\nu\uparrow}c^\dagger_{i+\tau,\nu\downarrow} + \text{H.c.}$, where $\tau = x \pm y$ and $\tau' = x \pm y \pm z$. In momentum space, the superconducting Hamiltonian reads $H_{\Delta,k} = \sum_{R\nu\mathbf{k}}(\Delta_{R\nu\mathbf{k}}c^\dagger_{R\nu\mathbf{k}\uparrow}c^\dagger_{R\nu-\mathbf{k}\downarrow} + \text{H.c.})$, with

$$\begin{aligned}
\Delta_{R\nu\mathbf{k}} &= 2\sum_\tau \cos\mathbf{k}_\tau \Delta^{R\nu}_{i,i+\tau} + 2\sum_{\tau'}\cos\mathbf{k}_{\tau'}\Delta^{R\nu}_{i,i+\tau'} \\
&= 4\cos k_x \cos k_y\left(\Delta^s_{xy} + 2\Delta_z \cos k_z\right) \\
&\quad - 4\Delta^d_{xy}\sin k_x \sin k_y, \quad (4)
\end{aligned}$$

where the self-consistent pairing order parameter $\Delta^{R\nu}_{i,i+\tau} = \frac{V_\tau}{2}\langle c^R_{i\nu\uparrow}c^R_{i+\tau,\nu\downarrow} - c^R_{i\nu\downarrow}c^R_{i+\tau,\nu\uparrow}\rangle$ can be solved numerically. Interestingly, the value of the superconducting pairing order within an Fe layer can be expressed as a linear combination of d-wave and s-wave pairing orders defined by $\Delta^{s,d}_{xy} = 0.5(\Delta^{R\nu}_{i,i+\hat{x}+\hat{y}} \pm \Delta^{R\nu}_{i,i+\hat{x}-\hat{y}})$ because the superconducting pairing order on $(\hat{x} + \hat{y})$-orientated links is different from that on $(\hat{x} - \hat{y})$-orientated ones. The interlayer pairing order is denoted Δ_z hereafter for short, and the paring potential $V_{xy,z} = 1.6$ for both intra- and interlayer superconducting pairing order. Here, it should be noted that when the pairing order parameter Δ_z approaches zero, the three-dimensional superconductivity will evolve into an exact two-dimensional superconducting system, and the pairing order $\Delta_{R\nu\mathbf{k}}$ has $s_\pm$ symmetry with the nodal lines located around $k_x = \pm\pi/2$ and $k_y = \pm\pi/2$. When the pairing order parameter Δ_z is increased to a finite value, such as $|\frac{-\Delta^s_{xy}}{2\Delta_z}| \leqslant 1$, some extra nodal points will penetrate into the hole pockets around Γ point.

In the numerical calculation, we set the distance between the nearest-neighbor Fe atoms and the hopping integral t_1 as

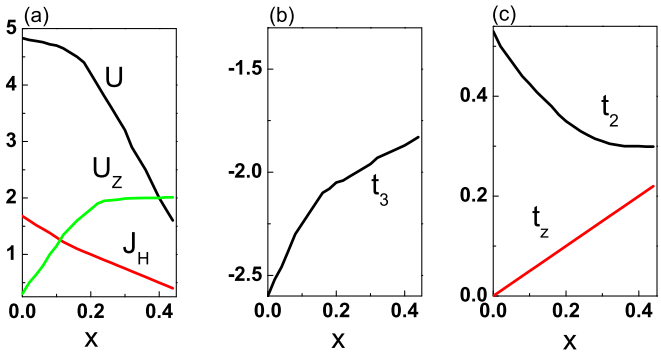

FIG. 2. Doping-dependent (a) Coulomb interactions including U, J_H, and U_z, and hopping energy parameters (b) t_3 and (c) t_2 and t_z.

the length and energy units, respectively. By self-consistently diagonalizing the 24×24 total Hamiltonian in momentum space, $H^0_{\rm tot}(k) = H_{t,k} + H_{\Delta,k} + H_{{\rm int},k} = \sum_n E_n \gamma_n^\dagger \gamma_n$, we obtain the eigenvalues and the corresponding eigenstates of the system, which can be used for further calculating the physical quantities, such as superfluid density and the local DOS. The unit cell is $128 \times 128 \times 128$ for the self-consistent calculation and $384 \times 384 \times 384$ for the calculations of superfluid density and band structure, as well as the DOS.

III. PHASE DIAGRAM AND LONDON PENETRATION DEPTH

Figure 2 shows the doping-dependent parameters used for the detailed calculations, including all hopping energies and interactions, $t_2, t_3, t_z, U, U_z, J_H$, smoothly varied under various doping concentrations. The variation of these parameters is constructed only to fit the experimental observations [7,12,28]. The numerically self-consistently calculated phase diagram is shown in Fig. 3(a), which is in quite good agreement with previous experimental observations [12,13,43]. The parent compound $BaFe_2As_2$ with antiferromagnetic order will be suppressed monotonously with increasing the doping concentration x. When the doping is increased beyond $x = 0.08$, the superconductivity emerges, as evidenced by the appearance of the intralayer and interlayer superconducting pairing

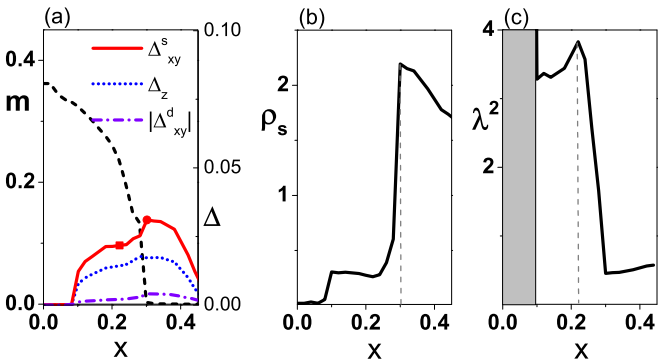

FIG. 3. (a) Doping-dependent magnetic order m, intralayer superconducting orders $\Delta^{s,d}_{xy}$, and interlayer superconducting order Δ_z for $BaFe_2(As_{1-x}P_x)_2$. (b) Superfluid density ρ_s versus doping level x. (c) Square of the penetration depth λ^2 versus x.

order parameters $\Delta^{s,d}_{xy}$ and Δ_z, and then the system enters the region where magnetism and superconductivity coexist until the doping concentrations reach $x = 0.3$. If we further increase the doping concentrations, the magnetism disappears, and the system becomes pure superconductivity. In Fig. 3(a), we also notice that both Δ^s_{xy} and Δ_z versus doping x display a clear dome-shaped superconductivity, and the values of Δ^s_{xy} and Δ_z reach their maximum at the point where magnetic order disappears. The absolute value of $|\Delta^d_{xy}|$ for the two different Fe sublattices is also shown in Fig. 3(a).

Next, we turn to discussing the behaviors of superfluid density based on the linear response approach. Assuming that, in the presence of a slowly varying vector potential along the x direction $A_x(r,t) = A(q,\omega)e^{i\mathbf{q}\cdot\mathbf{r}_i - i\omega t}$, all self-consistent mean-field calculations are unchanged in the framework of the linear response theory, only hopping energy terms should be modified by a Peierls phase factor, $c^\dagger_{i\sigma}c_{j\sigma} \to c^\dagger_{i\sigma}c_{j\sigma}\exp i\frac{e}{\hbar c}\int_{r_j}^{r_i}\mathbf{A}(\mathbf{r},t)\cdot d\mathbf{r}$. Then expanding the factor to the order of $\mathbf{A}^2$, the perturbed Hamiltonian reads $H' = -\sum_i A_x[eJ^P_x(r_i) + \frac{e^2}{2}A_xK_x(r_i)]$, with

$$K_x(r_i) = -\sum_{\nu\nu'\sigma\delta} t_{i,i+\delta}x^2_{i,i+\delta}(c^\dagger_{i\nu\sigma}c_{i+\delta,\nu'\sigma} + \text{H.c.}), \quad (5)$$

$$J^P_x(r_i) = -i\sum_{\nu\nu'\sigma\delta} t_{i,i+\delta}x_{i,i+\delta}(c^\dagger_{i\nu\sigma}c_{i+\delta,\nu'\sigma} - \text{H.c.}), \quad (6)$$

where $\delta = x, x\pm y, x\pm y\pm z$. The total current density $J^Q_x(r_i,t) = -\frac{\delta H'}{\delta A_x(r_i,t)}$ induced by an external magnetic field is the summation of the diamagnetic part K_x and the paramagnetic part J^p_x. The calculations of K_x are restricted to the zeroth order of $A_x(r_i)$, and that of $J^P_x(r_i)$ is restricted to the first order of $A_x(r_i)$, $\langle J^P_x(r_i)\rangle = -\frac{eA_x(r,t)}{N_s}\Pi(\mathbf{q},\omega)$, where $\Pi(\mathbf{q},\omega)$ is obtained from the analytic continuation of the current-current correlation $\Pi(\mathbf{q},i\omega) = \int_0^\beta d\tau e^{i\omega\tau}\Pi(\mathbf{q},\tau)$ in the Matsubara formalism. Here, $\Pi(\mathbf{q},\tau) = -\langle T_\tau J^P_x(\mathbf{q},\tau)J^P_x(-\mathbf{q},0)\rangle_0$, $J^P_x(\mathbf{q},\tau) = e^{\tau H_0}J^P_x(\mathbf{q})e^{-\tau H_0}$, $J^P_x(\mathbf{q}) = \sum_i e^{-i\mathbf{q}\cdot\mathbf{r}_i}J^P_x(r_i)$, and T_τ is the imaginary time ordering operator. In the quasiparticle basis, the paramagnetic current can be expressed as the summation of components $J^P_x(\mathbf{q}) = \sum_{m_1m_2}J^P_{m_1m_2}$, with $J^P_{m_1m_2} = \gamma^{\dagger\mathbf{k}}_{m1}\gamma^{\mathbf{k}+\mathbf{q}}_{m2}\Gamma^{\mathbf{k},\mathbf{k}+\mathbf{q}}_{m_1m_2}$. After some tedious but straightforward algebraic derivations, the concrete expression of Γ is derived. Using the equation of motion of Green's function, we obtain [24]

$$\Pi(\mathbf{q},i\omega) = \sum_{\mathbf{k}m_1m_2\sigma}\frac{\Gamma^{\mathbf{k},\mathbf{k}+\mathbf{q}}_{m_1m_2}\Gamma^{\mathbf{k}+\mathbf{q},\mathbf{k}}_{m_2m_1}[f(E_{\mathbf{k},m_1}) - f(E_{\mathbf{k}+\mathbf{q},m_2})]}{i\omega + (E_{\mathbf{k},m_1} - E_{\mathbf{k}+\mathbf{q},m_2})}, \quad (7)$$

where f is the Fermi-Dirac distribution function. Thus, the superfluid density weight measured by the ratio of the superfluid density to the mass is proportional to $\Pi(\mathbf{q},\omega)$ in the limit of zero frequency ω and momentum $\mathbf{q}$ [24,44–46] and is expressed as

$$\frac{\rho_s}{m^*} = -\langle J^Q_x(r_i,t)\rangle/e^2A_x(r_i) = \frac{1}{N_s}\Pi(q_x = 0, q_y \to 0, q_z \to 0, \omega = 0) - \langle K_x\rangle_0. \quad (8)$$

Figure 3(b) shows the superfluid density ρ_s as a function of doping concentration x across the whole phase diagram in

Fig. 3(a) at zero temperature. At underdoped concentration x around the parent compound system, the superfluid density ρ_s is zero, as expected from our intuitive knowledge that the system does not have superconducting order. As the doping concentration x increases, the superconductivity emerges, accompanied by the appearance of a finite value of ρ_s. If the doping concentration x is further increased, ρ_s changes to decrease its value slowly until $x = 0.22$, and then ρ_s further goes upward with a steep slope, displaying a sharp peak at $x = 0.3$ with the value of superfluid density being 8 times larger than that at $x = 0.22$. Reaching the maximal value of superfluid density ρ_s at $x = 0.3$ corresponds to the point of the disappearance of magnetic order in Fig. 3(a), denoted by the red dot in the curve of Δ^s_{xy}. Eventually, the superfluid density ρ_s decreases sharply and then tends to saturate to a finite value upon further increasing the doping concentration x.

In addition, a fundamental property of the superconducting state is the London penetration depth λ, parametrizing the ability of a superconductor to screen an applied magnetic field, which not only can be evaluated straightforwardly from the superfluid density ρ_s but also can be measured in experiments [21]. In general, ρ_s is described as the phase rigidity of a superconductor, and it may vanish before the superconducting energy gap diminishes with increasing temperature. In Fig. 3(c), we plot the square of the London penetration depth λ^2 as a function of doping concentration x. It is important to point out that the value of the London penetration depth λ^2 displays a sharp peak at $x = 0.22$ which corresponds to the minimal value of ρ_s and corresponds to the red square in the curve of Δ^s_{xy} in Fig. 3(a), and then it decreases sharply. Eventually, λ^2 becomes rather flat in the pure superconducting region. Compared with the experimental results [12], where the magnetic phase boundary corresponds to the sharp peak of λ^2, our numerical results show that the sharp peak in the penetration depth appears before the vanishing of the magnetic order. Such an anomalous peak in the London penetration depth has not been observed experimentally in other iron-based superconductors, and it leads to a conjecture about the presence of the QCP in $BaFe_2(As_{1-x}P_x)_2$.

The superconducting gap structure in the band representation $\tilde{\Delta}_k$ is derived from the 6×6 matrix Hamiltonian $H_{\Delta,k}$ of Δ_k (shorthand for Δ_{Rvk}) in the orbital space as $[\tilde{H}_{\Delta,k}] = [W]^\dagger[H_{\Delta,k}][W]^*$ when magnetic order is absent, with $[W]$ being the transformation matrix diagonalizing the 6×6 tight-binding Hamiltonian $H_{t,k}$, and the corresponding $\tilde{\Delta}_k$ are the diagonal elements of $[\tilde{H}_{\Delta,k}]$. However, for finite magnetic order the corresponding $[W]$ is a 12×12 matrix diagonalizing the Hamiltonian $H_{t,k} + H_{\text{int},k}$ including the interaction part. Figure 4 displays the behavior of $\tilde{\Delta}_k$ near the Fermi surface, where the navy points correspond to positive signs of $\tilde{\Delta}_k$ and the orange points are for the minus signs. Figure 4 shows that the gap structure in $x = 0.23$ has a finite value near the Fermi surface at all k_z, which is quite different from that in the $x = 0.18$ case where the node points exist. For a given doping level, a larger k_z corresponds to a smaller magnitude of the superconducting gap. It is important to point out that along the line of k_z, the superconducting gap will change signs from 0.5π to π when we do not consider the effect of magnetic order, which can be seen clearly in Fig. 4(c), where we set the magnetic order to zero. Therefore, we expect that in the region with the sudden drop in penetration depth the corresponding $\tilde{\Delta}_k$ will change its structure.

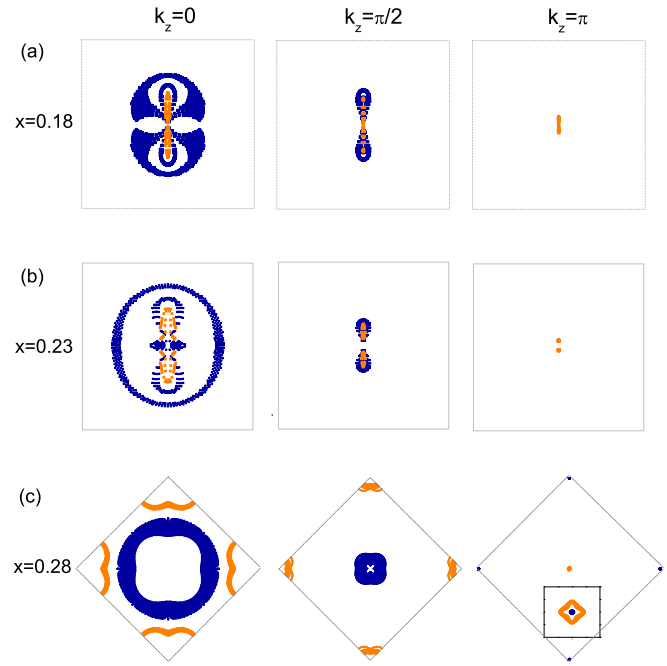

FIG. 4. Superconducting gap structure of the band space for different doping concentrations $x = 0.18, 0.23, 0.28$ near the Fermi surface. From left to right the plots correspond to $k_z = 0, \pi/2, \pi$, respectively. The inset in (c) is an enlargement of the z point. The gray lines are the corresponding first Brillouin zone.

IV. DOS AND FERMI SURFACE TOPOLOGIES

To clarify the nature of the emergence of an anomalous sharp peak in the penetration depth, we calculate the DOS for various doping concentrations x at zero temperature, as shown in Fig. 5. When the doping concentration is located in the region of $x \leqslant 0.22$, the calculated DOS displays a V-shaped structure with finite value at the Fermi level, implying the presence of nodal points in the superconducting energy gap. As the doping concentration x increases, the V-shaped DOS changes into a U-shaped structure at $x = 0.24, 0.26$ with a diminished DOS at the Fermi level; the plot for $x = 0.23$ is similar to that for $x = 0.24$, which we do not show here. When the doping concentration is increased beyond 0.28, the tip at zero energy reappears [see Fig. 5(e)]. Figure 5(f) shows a narrow V-shaped DOS feature in a pure superconducting region, suggesting the system is a nodal superconductor, which is in agreement with the previous ARPES measurement [28]. Therefore, comparing Fig. 5 with Fig. 3(c), we find that the phase transition of the changing pairing order parameter from nodeless to a nodal structure is responsible for the appearance of the sharp peak in the experimental measurement of the London penetration depth.

To further understand the nature of the emergence of the anomalous sharp peak in the London penetration depth, we also plot the DOS for $\Delta_z = 0$, a two-dimensional limited case, shown by the gray dashed lines in Fig. 5, where the interlayer interaction $V_z = 0$ is set to zero and the other interaction

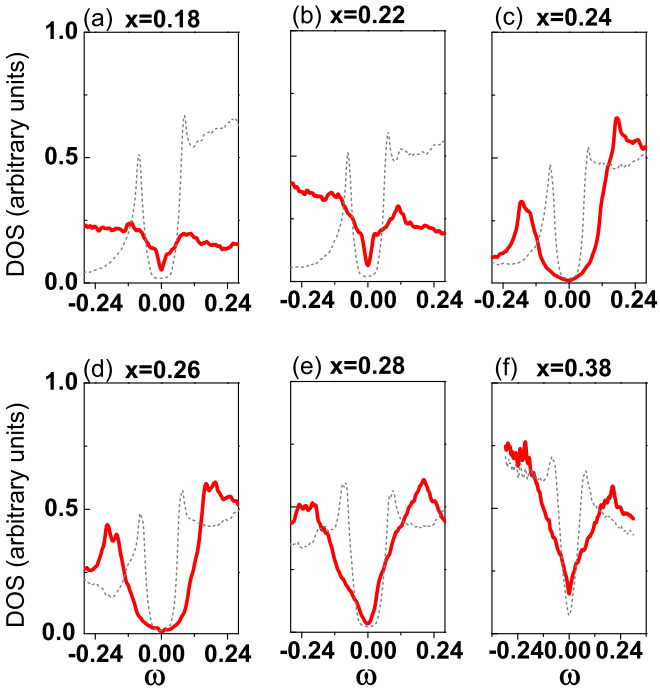

FIG. 5. (a)–(f) For $V_z = 1.6$, DOS as a function of energy at various doping concentrations $x = 0.18, 0.22, 0.24, 0.26, 0.28, 0.38$ are shown by the red lines, where the gray dashed lines represent the corresponding DOS for $V_z = 0$.

parameters remain the same as in Fig. 2. For this 3D interaction and two-dimensional superconducting order case, the system displays a U-shaped DOS for all doping concentrations from $x = 0.18$ to $x = 0.28$.

In the case where Δ_z is absent, the nodal-to-nodeless transition no longer exists since all the DOSs are U-shaped features. Although the resulting ρ_s and λ^2 still have a sharp peak as that in $V_z = 1.6$ case, which can be seen clearly in Figs. 6(b) and Fig. 6(c), a remarkable dip in the phase diagram of Δ^s_{xy} versus doping appears, which is ascribed to the presence of three-dimensional interaction. Figure 6(a) shows that Δ^s_{xy} drops to a minimum value suddenly at $x = 0.24$,

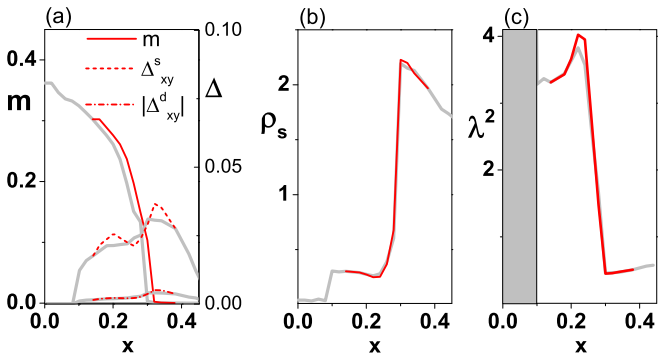

FIG. 6. In the doping region of [0.14,0.36], the red curves are doping-dependent physical quantities for the $\Delta_z = 0$ case. (a) Magnetic order m and superconducting orders $\Delta^{s,d}_{xy}$, (b) superfluid density ρ_s, and (c) the square of the penetration depth as a function of doping. The gray lines are the corresponding curves of $V_z = 1.6$ in Fig. 3.

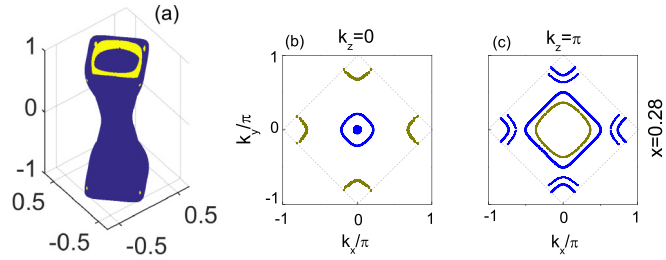

FIG. 7. (a) Three-dimensional plot of the two cylindrical shells around the Γ point for a dopant concentration of $x = 0.28$. (b) and (c) Counter plots of the Fermi surface at $k_z = 0$ and $k_z = \pi$, respectively. Blue points denote the plus signs of the corresponding superconducting pairing, and dark yellow points are for the minus signs.

destroying the dome-shaped superconductivity and leading to an unphysical anomalous penetration depth. A minimum pairing order corresponding to a maximal penetration depth is a reasonable result when there is no other phase transition. Furthermore, for two-dimensional dome-shaped iron-based superconductivity [24], the penetration depth does not show the sharp peak. Therefore, the experimental observation of a sharp peak in penetration depth having dome-shaped superconductivity stems from three-dimensional electron interactions accompanied by a transition from nodal to nodeless pairing.

In addition to analyzing the numerical data for superconducting pairing order parameters, we find a nodal circle in the inner hole pocket around the Γ point in the vicinity of $k_z = 0.86\pi$ for $x = 0.28$ and four nodal points in the outer hole pocket, which is shown in Fig. 7(a) with the boundaries of the two colors denoting the nodal points on the 3D Fermi surface topologies. For $k_z > 0.86\pi$, the superconducting pairing in the inner hole pocket changes sign, while the points on the outer pocket remain the same color as that of small k_z, which is quite different from $x = 0.18$ shown in Fig. 1(b). In order to unambiguously display the inner shape of Fermi surface topologies, Figs. 7(b) and 7(c) depict the contour plot of the Fermi surface for $k_z = 0$ and for $k_z = \pi$ at $x = 0.28$, respectively. For $k_z = \pi$ the superconducting gap has different signs on the outer and inner hole pockets, which is different from $x = 0.18$ but consistent with the inset of Fig. 4. It is worth pointing out that the small inner circle of the hole pocket around the Γ point in the Brillouin zone is easily immersed if the doping concentration is increased further. The larger k_z has a larger Fermi surface circle; however, the magnitude of the corresponding superconducting pairing is small, as shown in Fig. 4. Those calculations further solidify the nature of nodeless-to-nodal transition in doped $BaFe_2(As_{1-x}P_x)_2$, leading to the appearance of an anomalous sharp peak in the London penetration depth.

V. SUMMARY

In this paper, we constructed a three-dimensional tight-binding lattice model based on the facts from the penetration

depth and the ARPES experimental measurements. Taking the interlayer Coulomb interactions into account, the superconducting phase diagram and an anomalous sharp peak in the London penetration depth were evaluated and are entirely in good agreement with experimental observations. By verifying the DOS and the pairing order parameters as well as the Fermi surface topologies at various doping concentrations, we find that the QCP originates from the nature of three-dimensional interactions, leading to a phase transition from a nodeless to a nodal pairing symmetry. This finding provides significant insight into the understanding of the nature of the QCP that emerged in the London penetration depth experiment in the isovalent doped superconductor $BaFe_2(As_{1-x}P_x)_2$.

ACKNOWLEDGMENTS

This work was supported by the National Key Research and Development Programs of China (Grants No. 2017YFA0304204 and No. 2016YFA0300504), Nat Basic Research Program of China (Grant No. 2914CB921203), the National Natural Science Foundation of China (Grants No. 11625416, No. 11474064, No. 11674278, No. 11927807, and No. 11774218), Shanghai Municipal Government under the Grant No. 19XD1400700, the Natural Science Foundation of Shanghai of China (Grants No. 18JC1420402 and No. 19ZR1402600), and the Natural Science Foundation from Jiangsu Province of China (Grant No. BK20160094). W.L. also acknowledges the start-up funding from Fudan University.

[1] Y. Kamihara, T. Watanabe, M. Hirano, and H. Hosono, J. Am. Chem. Soc. **130**, 3296 (2008).
[2] H. Ding, P. Richard, K. Nakayama, K. Sugawara, T. Arakane, Y. Sekiba, A. Takayama, S. Souma, T. Sato, T. Takahashi, Z. Wang, X. Dai, Z. Fang, G. F. Chen, J. L. Luo, and N. L. Wan, Europhys. Lett. **83**, 47001 (2008).
[3] G. R. Stewart, Rev. Mod. Phys. **83**, 1589 (2011).
[4] A. Damascelli, Z. Hussain, and Z.-X. Shen, Rev. Mod. Phys. **75**, 473 (2003).
[5] C. C. Tsuei and J. R. Kirtley, Rev. Mod. Phys. **72**, 969 (2000).
[6] M. Rotter, M. Tegel, D. Johrendt, I. Schellenberg, W. Hermes, and R. Pöttgen, Phys. Rev. B **78**, 020503(R) (2008).
[7] H. Shishido, A. F. Bangura, A. I. Coldea, S. Tonegawa, K. Hashimoto, S. Kasahara, P. M. C. Rourke, H. Ikeda, T. Terashima, R. Settai, Y. Önuki, D. Vignolles, C. Proust, B. Vignolle, A. McCollam, Y. Matsuda, T. Shibauchi, and A. Carrington, Phys. Rev. Lett. **104**, 057008 (2010).
[8] S. Kasahara, T. Shibauchi, K. Hashimoto, K. Ikada, S. Tonegawa, R. Okazaki, H. Shishido, H. Ikeda, H. Takeya, K. Hirata, T. Terashima, and Y. Matsuda, Phys. Rev. B **81**, 184519 (2010).
[9] H. Suzuki, T. Kobayashi, S. Miyasaka, T. Yoshida, K. Okazaki, L. C. C. Ambolode, S. Ideta, M. Yi, M. Hashimoto, D. H. Lu, Z.-X. Shen, K. Ono, H. Kumigashira, S. Tajima, and A. Fujimori, Phys. Rev. B **89**, 184513 (2014).
[10] M. Dzero, M. Khodas, A. D. Klironomos, M. G. Vavilov, and A. Levchenko, Phys. Rev. B **92**, 144501 (2015).
[11] Y. Murakami, P. Werner, N. Tsuji, and H. Aoki, Phys. Rev. Lett. **113**, 266404 (2014).
[12] K. Hashimoto, K. Cho, T. Shibauchi, S. Kasahara, Y. Mizukami, R. Katsumata, Y. Tsuruhara, T. Terashima, H. Ikeda, M. A. Tanatar, H. Kitano, N. Salovich, R. W. Giannetta, P. Walmsley, A. Carrington, R. Prozorov, and Y. Matsuda, Science **336**, 1554 (2012).
[13] Y. Nakai, T. Iye, S. Kitagawa, K. Ishida, H. Ikeda, S. Kasahara, H. Shishido, T. Shibauchi, Y. Matsuda, and T. Terashima, Phys. Rev. Lett **105**, 107003 (2010).
[14] R. M. Fernandes, S. Maiti, P. Wölfle, and A. V. Chubukov, Phys. Rev. Lett. **111**, 057001 (2013).
[15] Z. Diao, D. Campanini, L. Fang, W.-K. Kwok, U. Welp, and A. Rydh, Phys. Rev. B **93**, 014509 (2016).
[16] M. P. Smylie, M. Leroux, V. Mishra, L. Fang, K. M. Taddei, O. Chmaissem, H. Claus, A. Kayani, A. Snezhko, U. Welp, and W. K. Kwok, Phys. Rev. B **93**, 115119 (2016).
[17] D. Chowdhury, B. Swingle, E. Berg, and S. Sachdev, Phys. Rev. Lett. **111**, 157004 (2013).
[18] J.-H. Dai, Q. M. Si, J.-X. Zhu, and E. Abrahams, Proc. Natl. Acad. Sci. **106**, 4118 (2009).
[19] M. A. Tanatar, K. Hashimoto, S. Kasahara, T. Shibauchi, Y. Matsuda, and R. Prozorov, Phys. Rev. B **87**, 104506 (2013).
[20] A. Levchenko, M. G. Vavilov, M. Khodas, and A. V. Chubukov, Phys. Rev. Lett. **110**, 177003 (2013).
[21] Y. Lamhot, A. Yagil, N. Shapira, S. Kasahara, T. Watashige, T. Shibauchi, Y. Matsuda, and O. M. Auslaender, Phys. Rev. B **91**, 060504(R) (2015).
[22] M. Dzero and A. Levchenko, Phys. Rev. B **98**, 054501 (2018).
[23] K. R. Joshi, N. M. Nusran, M. A. Tanatar, K. Cho, S. L. Bud'ko, P. C. Canfield, R. M. Fernandes, A. Levchenko, and R. Prozorov, arXiv:1903.00053.
[24] H. X. Huang, Y. Gao, J.-X. Zhu, and C. S. Ting, Phys. Rev. Lett. **109**, 187007 (2012).
[25] T. Nomoto and H. Ikeda, Phys. Rev. Lett. **111**, 167001 (2013).
[26] P. Walmsley, C. Putzke, L. Malone, I. Guillamón, D. Vignolles, C. Proust, S. Badoux, A. I. Coldea, M. D. Watson, S. Kasahara, Y. Mizukami, T. Shibauchi, Y. Matsuda, and A. Carrington, Phys. Rev. Lett. **110**, 257002 (2013).
[27] D. Chowdhury, J. Orenstein, S. Sachdev, and T. Senthil, Phys. Rev. B **92**, 081113(R) (2015).
[28] Y. Zhang, Z. R. Ye, Q. Q. Ge, F. Chen, J. Jiang, M. Xu, B. P. Xie, and D. L. Feng, Nat. Phys. **8**, 371 (2012).
[29] W. Li, J. X. Zhu, Y. Chen, and C. S. Ting, Phys. Rev. B **86**, 155119 (2012).
[30] K. Suzuki, H. Usui, and K. Kuroki, J. Phys. Soc. Jpn. **80**, 013710 (2011).
[31] D. Zhang, Phys. Rev. Lett. **103**, 186402 (2009); **104**, 089702 (2010).
[32] H. Huang, Y. Gao, D. Zhang, and C. S. Ting, Phys. Rev. B **84**, 134507 (2011).
[33] H. Huang, D. Zhang, Y. Gao, W. Ren, and C. S. Ting, Phys. Rev. B **93**, 064519 (2016).

[34] J.-X. Zhu, J.-P. Julien, Y. Dubi, and A. V. Balatsky, Phys. Rev. Lett. **108**, 186401 (2012).
[35] Y. Gao, J.-X. Zhu, C. S. Ting, and W.-P. Su, Phys. Rev. B **84**, 224509 (2011).
[36] J. Yong, S. Lee, J. Jiang, C. W. Bark, J. D. Weiss, E. E. Hellstrom, D. C. Larbalestier, C. B. Eom, and T. R. Lemberger, Phys. Rev. B **83**, 104510 (2011).
[37] Y. H. Su, C. Setty, Z. Q. Wang, and J. P. Hu, Phys. Rev. B **85**, 184517 (2012).
[38] P. A. Lee and X.-G. Wen, Phys. Rev. B **78**, 144517 (2008).
[39] I. I. Mazin, D. J. Singh, M. D. Johannes, and M. H. Du, Phys. Rev. Lett. **101**, 057003 (2008).
[40] T. Zhou, D. Zhang, and C. S. Ting, Phys. Rev. B **81**, 052506 (2010).
[41] Y. Gao, H. X. Huang, C. Chen, C. S. Ting, and W.-P. Su, Phys. Rev. Lett. **106**, 027004 (2011).
[42] A. M. Oleś, G. Khaliullin, P. Horsch, and L. F. Feiner, Phys. Rev. B **72**, 214431 (2005).
[43] D. Hu, X. Lu, W. Zhang, H. Luo, S. Li, P. Wang, G. Chen, F. Han, S. R. Banjara, A. Sapkota, A. Kreyssig, A. I. Goldman, Z. Yamani, C. Niedermayer, M. Skoulatos, R. Georgii, T. Keller, P. Wang, W. Yu, and P. Dai, Phys. Rev. Lett. **114**, 157002 (2015).
[44] T. Das, J. X. Zhu, and M. J. Graf, Phys. Rev. B **84**, 134510 (2011).
[45] D. J. Scalapino, S. R. White, and S. C. Zhang, Phys. Rev. B **47**, 7995 (1993).
[46] L. Liang, T. I. Vanhala, S. Peotta, T. Siro, A. Harju, and P. Törmä, Phys. Rev. B **95**, 024515 (2017).